Absolute photometric calibration of IRAC -- Lessons learned using nine years of flight data

S. Carey[a,*], J. Ingalls[a], J. Hora[b], J. Surace[a], W. Glaccum[a], P. Lowrance[a], J. Krick[a], D. Cole[a], S. Laine[a], C. Engelke[c], S. Price[c], R. Bohlin[d], K. Gordon[d]

[a]Spitzer Science Center, MS 220-6, California Institute of Technology, Pasadena, CA, USA, 91125;
[b]Harvard-Smithsonian Center for Astrophysics, 60 Garden Street, Cambridge, MA, USA, 02138;
[c]Institute for Scientific Research , 400 St. Clements Hall, Boston College, 140 Commonwealth Ave. Chestnut Hill, MA, USA, 02467;
[d]Space Telescope Science Institute, 3700 San Martin Drive, Baltimore, MD, 21218

ABSTRACT

Significant improvements in our understanding of various photometric effects have occurred in the more than nine years of flight operations of the Infrared Array Camera aboard the *Spitzer* Space Telescope. With the accumulation of calibration data, photometric variations that are intrinsic to the instrument can now be mapped with high fidelity. Using all existing data on calibration stars, the array location-dependent photometric correction (the variation of flux with position on the array) and the correction for intra-pixel sensitivity variation (pixel-phase) have been modeled simultaneously. Examination of the warm mission data enabled the characterization of the underlying form of the pixel-phase variation in cryogenic data. In addition to the accumulation of calibration data, significant improvements in the calibration of the truth spectra of the calibrators has taken place. Using the work of Engelke et al. (2006), the KIII calibrators have no offset as compared to the AV calibrators, providing a second pillar of the calibration scheme. The current cryogenic calibration is better than 3% in an absolute sense, with most of the uncertainty still in the knowledge of the true flux densities of the primary calibrators. We present the final state of the cryogenic IRAC calibration and a comparison of the IRAC calibration to an independent calibration methodology using the HST primary calibrators.

Keywords: infrared detectors, space telescopes, *Spitzer* Space Telescope, IRAC, photometric calibration

1. INTRODUCTION

The InfraRed Array Camera[1,2] (IRAC) aboard the *Spitzer* Space Telescope[3] has been providing high quality science data since the start of nominal operations on 01 December 2003 until the end of the cryogenic mission on 15 May 2009 and from the start of the warm science operations[4] on 27 July 2009 to the present. IRAC provides moderate resolution (1.6-2.0″), broad band (R~4) mid-infrared photometry in four passbands (3.6, 4.5, 5.8, 8.0 μm) sharing two 5′× 5′ fields of view. IRAC has a good combination of mapping efficiency (240 square degrees of the Galactic plane past the confusion limit in ~400 hours) and sensitivity (~100 nJy extragalactic confusion limit in ~10 hours). For the warm mission, the 3.6 and 4.5 μm (InSb) arrays operate with essentially the same sensitivity as during cryogenic operations while the longer wavelength (Si:As) arrays have too much dark current to be used at the warm operating temperature of 28.7 K.

IRAC has been used to make important discoveries such as the first robust detection of water in an exoplanet atmosphere[5], first measurement of the longitudinal temperature profile of a hot Jupiter exoplanet[6], mass measurements of massive clusters at redshifts of z ~ 2[7] that constrain the formation of structure in the early universe and characterization of the age and star formation of the highest redshift galaxies known[8,9].

Many of the science drivers for IRAC require modest absolute photometric accuracy of ~10% and in some cases only require good relative (between IRAC photometric band) accuracy. In particular, exoplanet science is insensitive to the absolute calibration but requires relative photometric precisions of <100 ppm. IRAC supplies extremely stable photometry[10] largely due to the great thermal stability of the instrument with the temperature of the arrays controlled to

---

[*] carey@ipac.caltech.edu; phone 1-626-395-8796; ssc.ipac.caltech.edu

<3mK. The demonstrated stability of the instrument permits use of the entirety of the history of calibration data for the purposes of trending systematic effects and providing the absolute photometric calibration of IRAC.

Significant science drivers do exist for high absolute photometric accuracy. In particular, use of type Ia supernova to well constrain the dark energy equation of state requires absolute photometric calibration of order 1%[11]. IRAC is being used to measure the Hubble constant to an accuracy of ~2%[12] and further improvements, if possible, will highly constrain the mass of neutrinos and the number of relativistic particle families. Investigations of the evolution of the planetesimal disks in analogs of the early solar system[13] including systems with dust production consistent with a late heavy bombardment phase are limited by the absolute calibration of mid-infrared measurements of the dust excess over the photospheric emission. Complementary studies of remnant disks[14] around white dwarf stars that provide information on the end stages of solar type systems are similarly constrained by the absolute photometric accuracy of the measurement. It is probable that additional significant science drivers will require excellent absolute photometric accuracy as the field evolves. In addition, ensuring the best possible calibration of IRAC is essential for the legacy value of the data when used in conjunction with forthcoming observations from JWST and other future observatories.

The remainder of this contribution describes the improvements we have made to the absolute calibration of IRAC using the data and knowledge obtained from more than nine years of flight data. Section 2 describes the calibration methodology and the differences from our original calibration[15]. In Section 3, we examine the systematic effects that need to be considered when calibrating IRAC. The final absolute calibration for the cryogenic data is presented in Section 4 along with a comparison to an independent calibration using HST standards. A summary and comments on future directions are given in Section 5.

2. METHODOLOGY

The absolute calibration of IRAC is determined by comparing the measured flux densities of periodic observations of a set of calibration stars in engineering units of data numbers per second with predictions of the expected flux density in Jy at the effective wavelength of the channel to obtain the absolute calibration scaling factor[15].

$$C' = \overline{\left(\frac{F^* * K^*}{R_{OBS}}\right)}, \tag{1}$$

where C' is the scaling factor, R_{OBS} is the measured flux density in the default aperture size in units of DN Hz, F^* is the expected flux density of the calibrator at the effective wavelength of the detector and K^* is the color correction for the calibration star spectral energy distribution. Instead of removing the previous calibration to return the preocessed data to units of DN Hz, we actually determine a correction factor from the previous calibration, $C_{new} = Q \times C_{old}$. As previously, a fiducial source spectrum of $F_\nu = F_{\nu0} (\nu/\nu_0)^{-1}$ is the convention so that the color correction is

$$K = \frac{\int (F_\nu/F_{\nu_0})(\nu/\nu_0)^{-1}R \, d\nu}{\int (\nu/\nu_0)^{-2}R \, d\nu}, \tag{2}$$

where R is the relative spectral response. The effective wavelength of the bandpass, $\lambda_0 = (c/\nu_0)$ is chosen to minimize K, that is,

$$\lambda_0 = \frac{\int \lambda \nu^{-1} R \, d\nu}{\int \nu^{-1} R \, d\nu}. \tag{3}$$

The scaling factor is converted into units of surface brightness (MJy/sr) by dividing by the average pixel size of the detector (~1.22″ → 3.50 ×10⁻¹¹ sr). The photometry is measured using standard aperture photometry on the basic calibrated data (BCD) produced by the Spitzer Science Center pipeline. Source centroids are determined using the center of light in a 7 x 7 pixel square aperture subtracting a background determined from the mean of a 6 pixel square background annulus offset by 3 pixels from the source aperture. For the original calibration, an aperture ten pixels in radius was used with a 12-20 pixel background annulus. The aperture photometry is performed using the 1st moment centroids with the aper.pro IDL astrolib procedure using the /EXACT and /FLUX keywords. The BCD pipeline corrects the data for instrumental signatures such as per-pixel bias, flat-field variations and linearizes the data. In addition, the
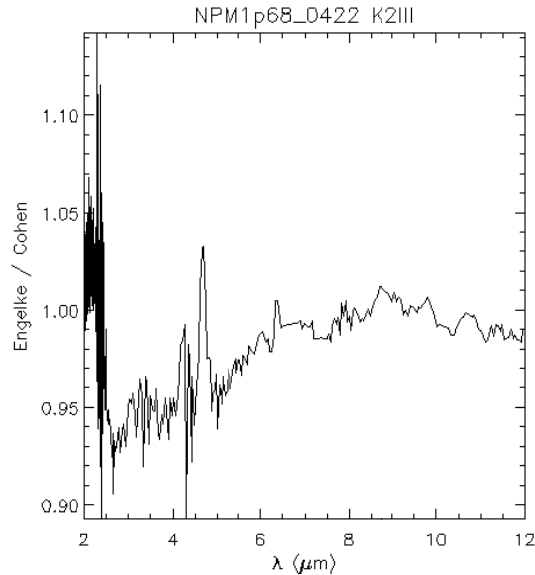
Figure 1. Ratio of predicted spectral energy distributions for the IRAC primary calibrator, NPM1+68.0433 for the original template from Cohen et al. (2003) and the one used for the final calibration from Engelke et al. (2006). For most of wavelength coverage of IRAC the original Cohen templates are brighter than the revised templates of Engelke.

images are flagged for radiation hits and other anomalies. Photometry is not performed on images that have anomalous data within the source aperture. As the calibration star observations are well-dithered and use integration times so that each measurement is in the linear response of the detectors (peak pixel filled to a well depth of 1/3 to 1/2 full), the uncertainty in the photometry due to uncertainties in the basic calibration are much less than 1% and the uncertainties are dominated by photon noise and the photometric systematics discussed in section 3.

The photometric systematics are corrected by applying scaling factors based on x, y position on the focal plane in all channels and correcting for the intra-pixel gain variation as a function of offset from pixel center for the 3.6 and 4.5 μm arrays. The mode of the corrected flux densities is measured for each calibrator and compared to predicted flux density for that calibrator to determine the update to the conversion factor, Q_i. We found that the mode was marginally more robust than the median or mean against outliers caused by low-level radiation hits.

Four stars of spectral type A0V-A3V and six stars of spectral type K0III-K2III comprise the primary calibrators for IRAC. For the AV stars, truth templates[16] were constructed by fitting Kurucz models to 2MASS, MSX and IRAS photometry. The KIII templates[17] were made by fitting synthetic spectra derived from ISO data of the same subclass of star to 2MASS, MSX and IRAS photometry. The individual Q_i values are averaged for the each class of calibrator and then the AV and KIII average Qs are averaged together to determine the update to the previous calibration for each IRAC channel.

2.1 Differences from the Reach et al. (2005) calibration

There are three major differences between the latest calibration and our previous calibration[15]. The most significant difference is the inclusion of the KIII calibrators in determining the flux conversion factor. In our earlier analysis, we rejected the K giants as there was a significant discrepancy between the scaling factors determined using the A dwarfs and K giants, 7.3, 6.5, 3.6 and 2.1% at 3.6, 4.5, 5.8 and 8.0 μm, respectively. We reasoned that the spectral features in the mid-infrared made it more difficult to determine the truth flux estimates for the K giants. This reasoning was validated with the production of improved templates[17], which significantly reduced the calibration discrepancy between AV and KIII stars. As discussed in section 4, the discrepancy is now less than 2% in all bands suggesting that both types of calibrators have similar systematic uncertainties at this point.

Figure 1 displays the significant differences between the two versions of KIII templates. In general, the earlier templates are brighter in the IRAC passbands with more significant differences for shorter wavelengths. Limited observations on
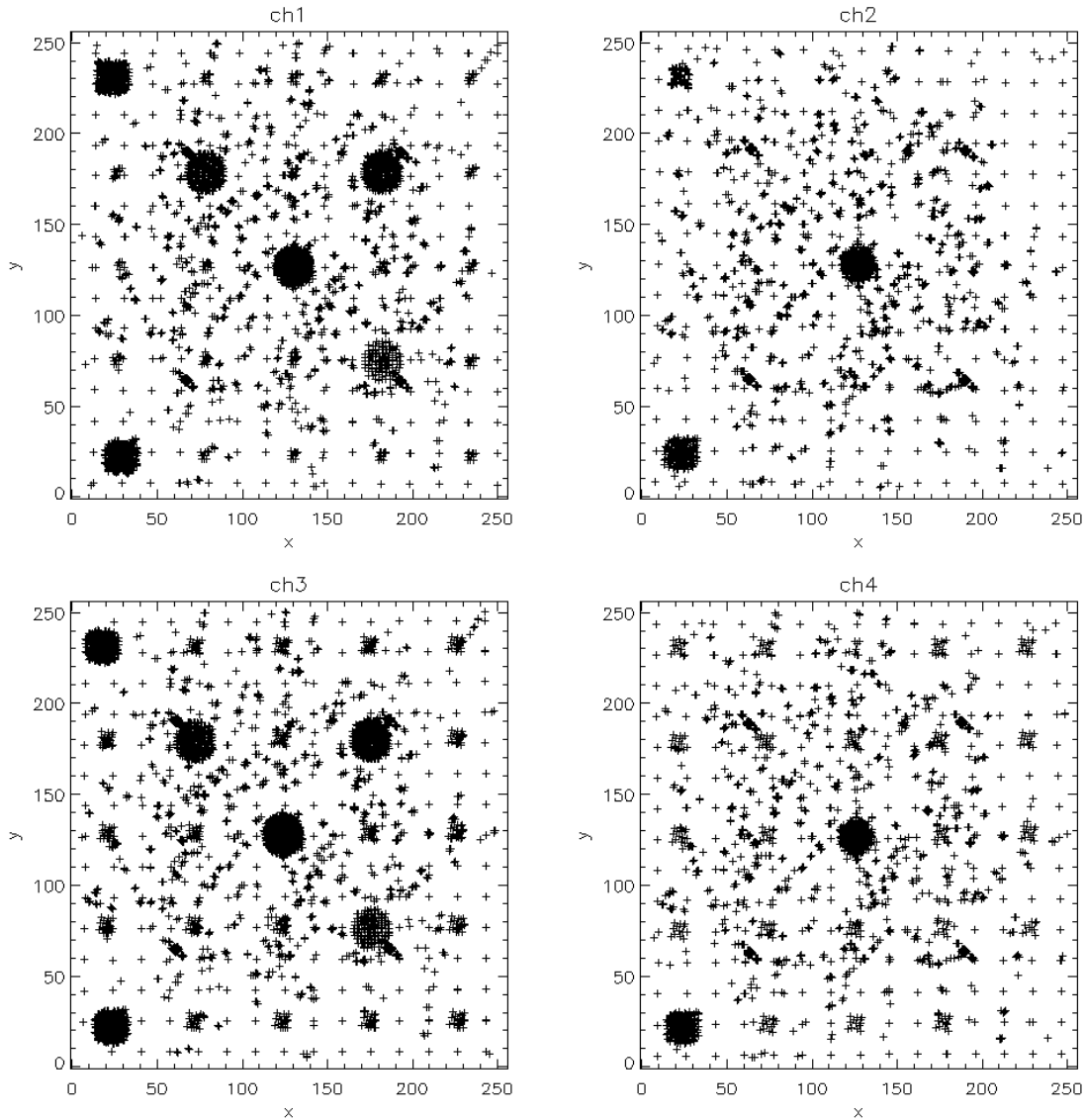
Figure 2. Locations on the focal planes of calibration star observations used for the final calibration plot as a function of x,y pixel position counting from 0 to 255. Clockwise from top left corner, 3.6, 5.8, 8.0 and 5.8 μm. In addition to fully sampling each focal plane, multiple sub-pixel offsets have been observed for most of the positions.

the IRTF with SpeX confirm this result, although the more recent Engelke models also do not fully agree with the SpeX data; however, the differences appear to be within the calibration uncertainties of the ground-based data.

The second significant modification was the incorporation of a two-dimensional function to remove intra-pixel gain variations at 3.6 and 4.5 μm. Detailed analysis[18] of staring mode data for warm mission exoplanet observations and our standard focal plane mapping data during the warm instrument characterization revealed that the photometric variations due to position relative to the center of a pixel are reasonably fit by a 2d Gaussian function in Δx and Δy, the offsets from the center of the pixel. The expectation was that the cryogenic data has intra-pixel gain variations with the same functional form but the amplitude of the effect is less due to the lower temperature that arrays were operated at.

The third modification is the use of updated spectral response curves which are the array average of the grid of response curves determined over the arrays considering the tilt of the filters[19, 20]. The last modification changes the effective wavelengths of the arrays from 3.550, 4.493, 5.731, 7.872 μm to 3.544, 4.487, 5.710, 7.841 μm, a modification of less than 0.4% in all passbands. In addition, the normalization of the flat-field and array location dependent corrections were
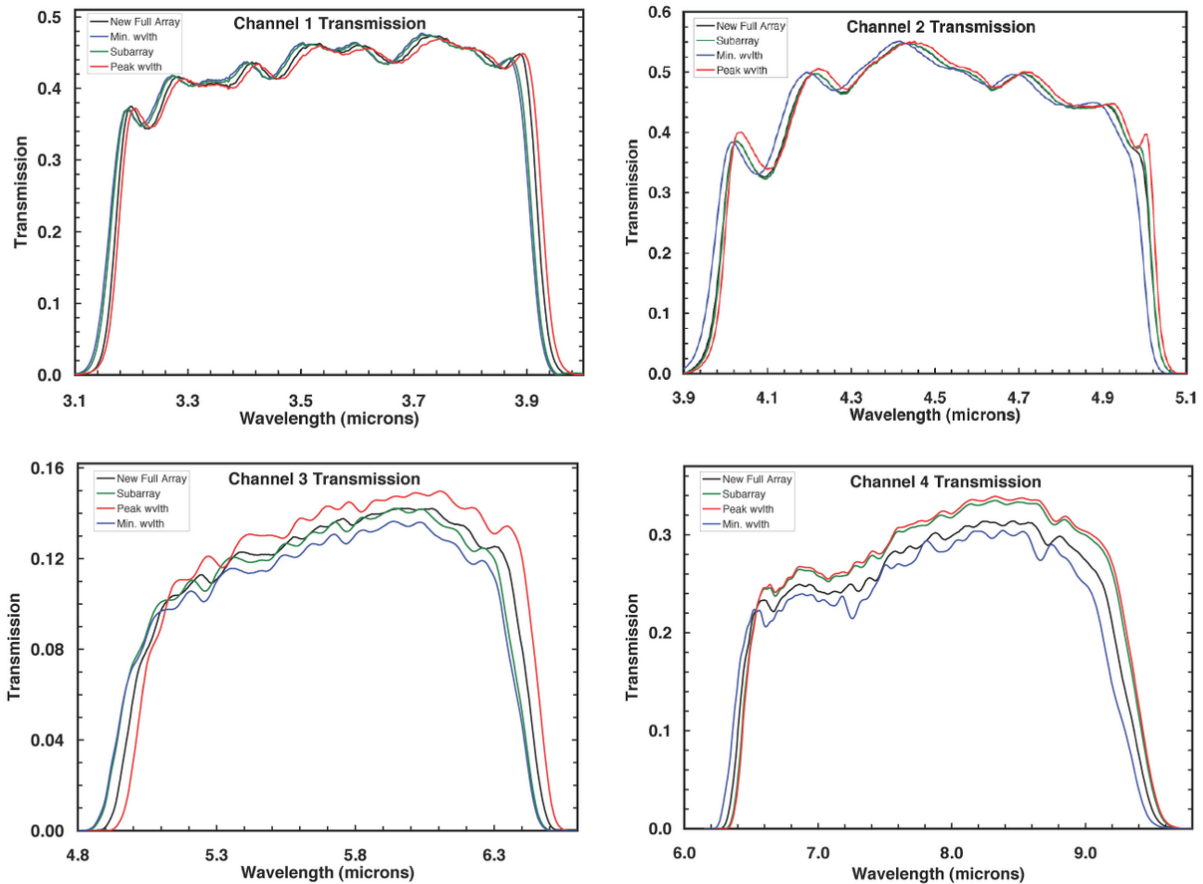
Figure 3. Representative spectral response curves for each channel. The blue and red curves are the maximum and minimum wavelength shift due to the change in angle of incidence through the filters. The black curves are the new average response curves used for the final absolute calibration. The green curve displays the response for the center of the subarray field of view for comparison.

changed to be averages over the entire array instead of an average over a more restricted region for the flat-field and using the photometric value at the array center to normalize the location dependent correction. Array averages were better enabled by the accumulation of the entire calibration dataset during the cryogenic mission lifetime and in the case of the location-dependent correction make photometry more robust even if the correction is not applied.

The initial calibration was done using observations which placed the calibration stars on five specific places on the array, the array center and four positions approximately halfway from the array center to the array edge. For the final calibration, we expanded the type of observation used to include all useful measurements of the calibration star including the focal plane mapping, final focus checks and PRF measurements as well as later calibration star observations that more fully sampled locations on the array as well as many intra-pixel phases. We were able to revise the strategy as the photometric calibration was exceedingly stable with time; hence, we did not have to acquire as much data to verify the stability later in the mission. Figure 2 displays the locations of the photometric points used for the final cryogenic calibration. Many of the pixels are sampled multiple times at many pixel phases.

The aperture size used for the final analysis was reduced to a 3 pixel aperture with a 3-7 pixel background annulus. Aperture corrections of 1.1257, 1.1226, 1.1356 and 1.2255 at 3.6, 4.5, 5.8 and 8.0 µm, respectively, were applied to place the photometry on the same scale as the original calibration. The use of a smaller aperture increased the number of available photometric points particularly for the Si:As arrays.

With the exception of the incorporation of the updated truth templates for the K giants, none of the modifications in our absolute calibration methodology should shift the calibration. However, due to the change in normalization and slight
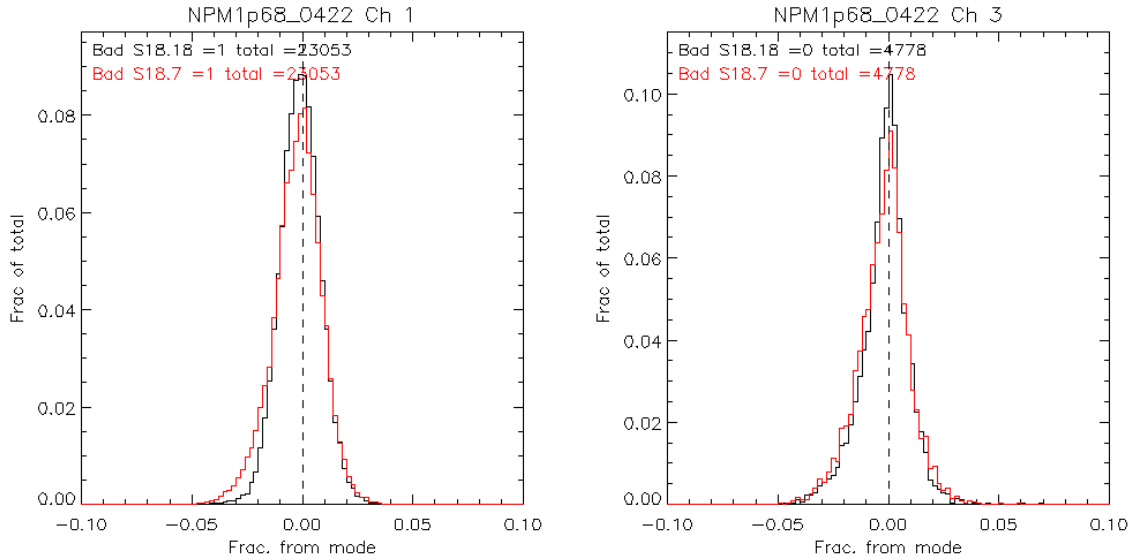
Figure 4. Improvement in noise distributions between final processing (black, S18.25) and previous pipeline versions (S17 and earlier, red). The left panel plots the distribution of calibration star observations for one of the primary calibrators at 3.6 μm. The right hand panel displays a similar plot at 5.8 μm. The results are similar between 3.6 and 4.5 μm and 5.8 and 8.0 μm where the 3.6 μm data has the most reduced scatter due to the improved intra-pixel gain correction used.

shift in effective wavelength, the final flux conversion factors are not directly comparable to the Reach et al. (2005) values as there is about a 2% shift in flux conversion value due to the change in the normalization of the array location-dependent photometric correction and the slight shift in effective wavelength of the filters using the revised bandpass functions displayed in Figure 3.

3. INSTRUMENT PHOTOMETRIC SYSTEMATICS

IRAC photometry has two significant instrumental systematics that need to be corrected for. The first effect is due to the variation in spectral response (as shown in Figure 3) as a function of position on the focal plane due to variations in path length through the bandpass filters. The second effect is the variation in the effective response of a pixel depending on the position of a point source on that pixel. The final corrections developed to remove these systematics reduce the scatter in the photometry of calibration stars, but do not significantly modify the modes of the distributions as shown in Figure 4. In particular, the noise in the 3.6 μm data is significantly improved due to the greatly improved intra-pixel gain variation (see Section 3.2)

3.1 Array location dependent photometric correction

The effect is amplified for sources with spectral energy distributions that decrease with wavelength as the images are flat-fielded using the Zodiacal light and the most significant effect due to the varying path lengths through the filters is a shift in the location of the edges of the spectral response functions. As the flat-field effectively removes the variation for red sources, it amplifies the effect for blue sources. The variation on the focal planes has a similar appearance for the 3.6 and 4.5 μm arrays and the 5.8 and 8.0 μm arrays as the InSb arrays have similar angles of incidence through their filters and the Si:As arrays likewise have similar angles of incidence although the photometric variation is flipped about the x-axis for the 5.8 and 8.0 μm arrays.

As in previous work[15,19] we model the photometric variation as a 2nd order polynomial in x and y pixel coordinates. Figure 5 displays the best fit models which have a similar appearance to the change in effective wavelength across the arrays[20]. The correction function, $L(x, y) = F_{CORR} \times F(x, y)$ that we use is

$$L(x, y) = L_0 + L_1 x_c + L_2 y_c + L_3 x_c y_c + L_4 x_c^2 + L_5 y_c^2, \qquad (3)$$

Table 1. Array location dependent photometric correction coefficients.

Band	L_0	L_1	L_2	L_3	L_4	L_5
3.6	0.98866790	-2.5460463e-05	-4.5413791e-05	-3.7748392e-07	9.6670990e-07	1.1259718e-06
4.5	0.97713769	0.00016023137	0.00010671203	6.1546421e-07	2.3478283e-06	1.8726664e-06
5.8	0.98318195	-0.00044891858	5.7375573e-05	3.5613363e-07	1.9036209e-06	1.1912425e-06
8.0	0.98239745	0.00020132123	-1.9285260e-05	-3.7193490e-07	1.4509036e-06	1.8131923e-06

where x_c and y_c are the integer pixel coordinates of the source centroid relative to array center, F_{CORR} is the corrected flux density and $F(x, y)$ is the measured flux density for a source with given position on the array. Table 1 lists the coefficients of the corrections used for the cryogenic mission for each array. Comparing our final correction to the Hora et al. (2008) version there are only very slight differences in the correction as both corrections are normalized so that the array average correction is unity.

3.2 Intra-pixel gain variations

This photometric variation called a pixel-phase effect or intra-pixel gain variation only affects the 3.6 and 4.5 μm data. The variation is due to non-uniform response in each pixel coupled with the undersampled PSF at these wavelengths. The Si:As arrays do not exhibit this effect in any measurable way.

In Reach et al. (2005), the effect was modeled as the measured flux decreasing with distance from the center of the pixel. With the accumulation of more calibration data and the identification of the same effect but with larger magnitude in the warm mission, we have been able to refine the functional fit. In addition, using the functional fit, we can apply a correction to the 4.5 μm cryogenic data which has a small (<1%) yet measurable intra-pixel gain variation. From analysis of the warm mission data we know that the functional form used, a 2d Gaussian with peak slightly offset from the pixel center, generally fits the gain variation, but low level modulation (~500 ppm) with periodicity of ~0.05 pixels still remains[18]. In detail the functional form depends on the particular pixel. The corrections we apply are determined from fitting the functional form to entire calibration star dataset for each channel (see Figure 2) and correct the photometry of an individual sample to better than 1% for most pixels and pixel-phases.

The correction function, $P(\Delta x, \Delta y) = F'_{CORR} \times F_{CORR}(\Delta x, \Delta y)$ applied to the data is

$$P(\Delta x, \Delta y) = F_x e^{\frac{-\delta x^2}{2\sigma_x^2}} + F_y e^{\frac{-\delta y^2}{2\sigma_y^2}} + F_0, \qquad (3)$$

where $\delta x = x - \text{fix}(x) - x_0$, $\delta y = y - \text{fix}(y) - y_0$ are the fractional pixel offsets from the peak response phase (x_0, y_0), F_x, F_y are the amplitude of the gain variation, σ_x^2, σ_y^2 are the variances in the width of the gain variation, and F_0 is an overall normalization. $F_{CORR}(\Delta x, \Delta y)$ is the photometry of an individual measurement corrected for the array location-dependent photometric variation. Table 2 lists the best fit parameters for the array average intra-pixel gain for the cryogenic data. Figure 6 demonstrates the model fit to the 3.6 μm photometry along with the residuals to the photometry after the fit.

Table 2. Intra-pixel gain variation coefficients.

Band	F_x	F_y	X_0	Y_0	σ_x	σ_y	F_0
3.6	0.018823169	0.030359022	0.091603768	0.0067795815	0.17107575	0.16949466	0.97909886
4.5	0.010250904	0.0091393800	0.040266280	0.12475250	0.17673946	0.27301699	0.98964462

The resultant photometry of calibration stars after correction for the photometric effects is extremely stable. Figure 7 displays the time series of photometry for the calibration star, KF06T2, a K1.5III star, at 3.6 μm. As with the other calibration stars there is no apparent trend in the photometry with time. Fits of a linear trend with time suggest there is no variation at a significance level of 0.01% over the course of the cryogenic mission. No apparent trend with time exists for the other arrays as well with the exception that the 5.8 μm calibration was slightly different for the first 8 weeks of

science operations and changed after the array was routinely annealed. The calibration of the other arrays also changed but by less than 1% when they were also routinely annealed starting earlier in the mission (prior to the end of IOC).
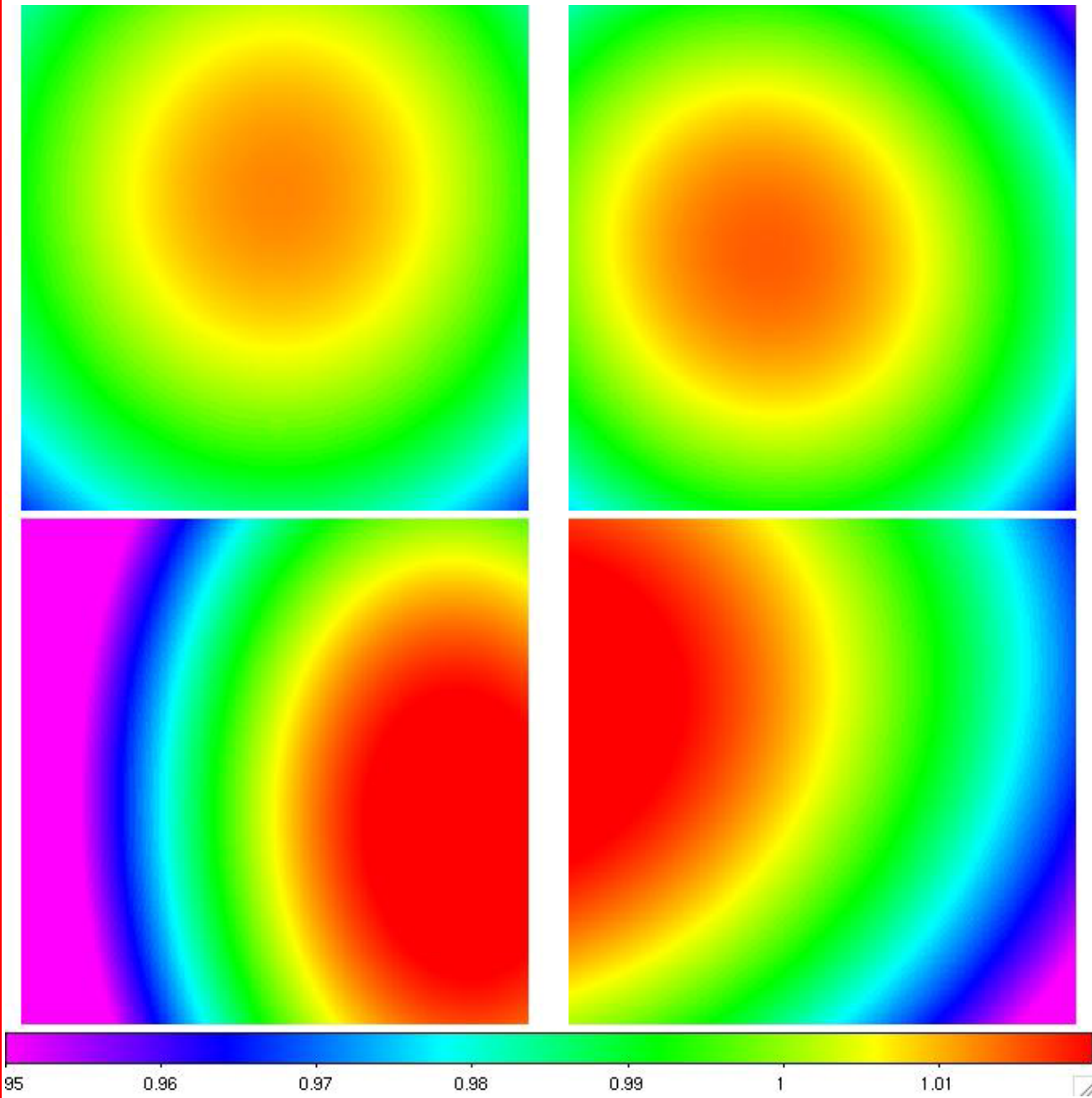

Figure 5. Maps of the dependence of photometry on location for each of the four arrays. Clockwise from top left are the 3.6, 4.5, 8.0 and 5.8 μm arrays, respectively. The InSb arrays have similar maps due to similar incoming ray angles as both InSb arrays are fed light reflected off the beamsplitter. Likewise, the Si:As arrays have a similar map pattern (though reflected) as the light is transmitted through the beamsplitters to those arrays.
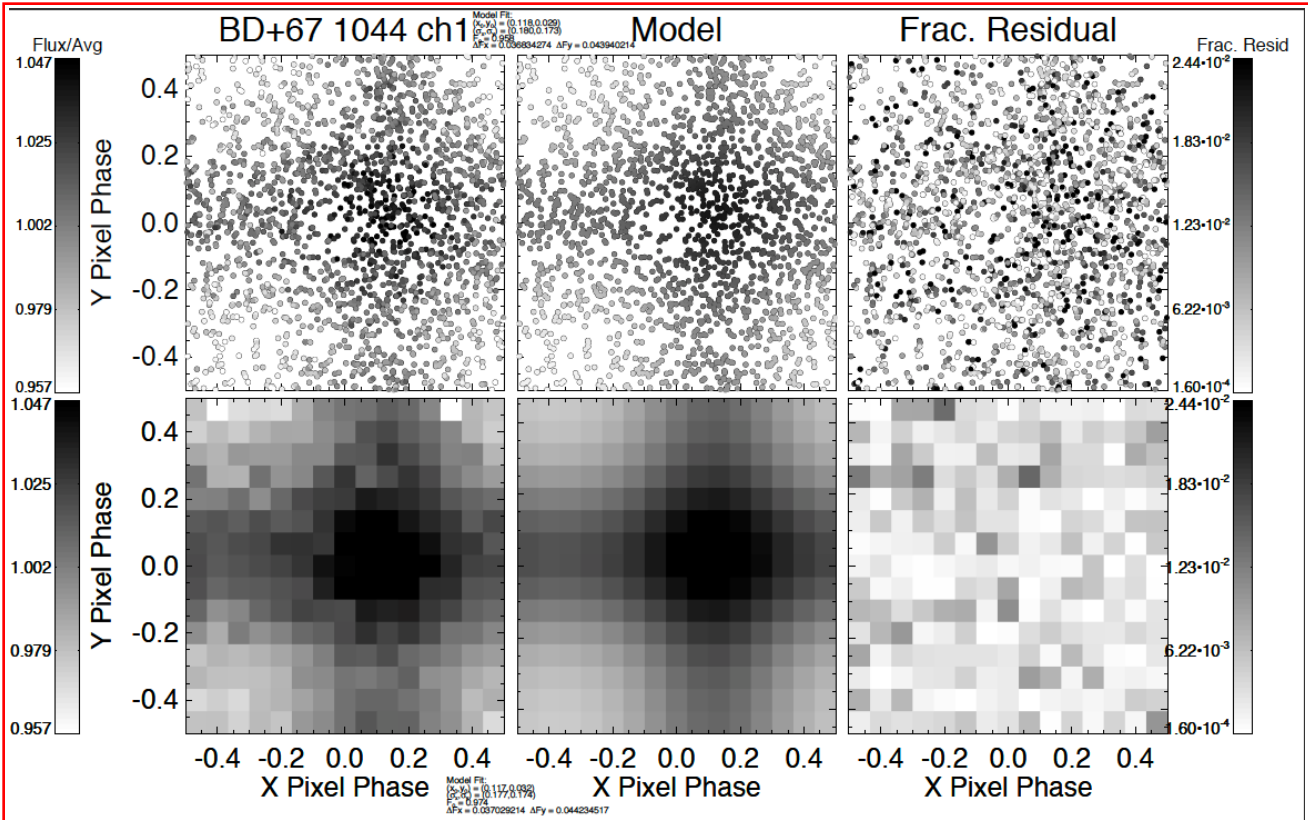
Figure 6. Measurement versus model of 3.6 μm cryogenic intra-pixel gain variation. The top panels display the individual photometric measurements used to map the gain variation. The lower panels display the binned photometry (left panel), model fit to the data (middle panel) and residual gain variation after fit (right panel). Photometric variations in excess of 4% are reduced to below 1% after applying the correction.
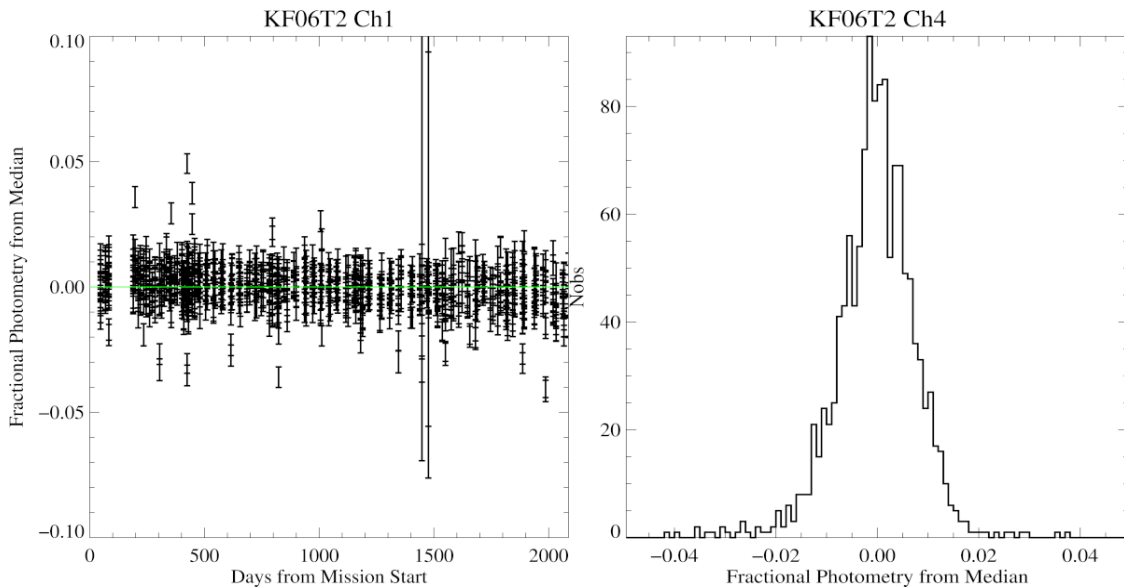

Figure 7. The left panel displays the relative variation in photometry for one calibration star at 3.6 μm over the course of the cryogenic mission. There is no trend in time to better than the 0.1% level. Right hand panel displays the distribution of fluxes at 8.0 μm for the same star for the cryogenic mission. The distribution is consistent with the expected photon noise of the observations.

4. ABSOLUTE CALIBRATION ACCURACY

We present the final cryogenic calibration values in Table 3. As previously[15], the formal uncertainty is dominated by the quoted 1.5% uncertainty in the calibration of the fundamental calibrators, Vega and/or Sirius used to tie the photometry of the primary calibrators used to an absolute physical scale. The uncertainty in the fundamental calibrators which tie measurements of celestial sources to NIST ground standards is the limiting parameter in improving the absolute calibration of space-based photometers.

The formal uncertainties in the flux conversion due to the measurement error of the calibration stars is now vanishingly small (<0.01%) as expected for the >10,000 photometric measurements used for each IRAC band. While the flux conversion value determined for any given star is determined with very high precision, there exists significant scatter between the flux conversion values derived per star. The formal measurement uncertainty due to the scatter in the flux conversions determined from the individual stars is ~0.6%. This uncertainty is a measure in the error in the underlying spectral templates used; however, it does not consider any systematic biases in those templates. A more robust estimate of the uncertainty in the flux conversion due to imperfect knowledge of the spectral energy distributions (templates) assumed is to examine the difference between the flux conversion calculated using the A dwarfs and the K giants separately. The flux conversions from the A stars are smaller (making sources less bright for a given measured DN/s value) by more than 1% at 3.6, 4.5 and 8.0 μm and ~0.5% larger at 5.8 μm. Root-sum-squaring the measurement uncertainty, the uncertainty in the fundamental calibrator and the bias between the AV and KIII flux conversion determinations, the formal uncertainty in the final flux conversion is 2.4, 2.0, 1.7 and 2.1% at 3.6, 4.5, 5.8 and 8.0 μm, respectively.

An independent check[21] on the IRAC calibration was done using IRAC observations of calibrators from the HST CALSPEC database. The sources in the CALSPEC database observed were a set of seven AV stars, three G0V stars and four white dwarfs. The HST calibration is based on the white dwarfs with the other sources used as secondary calibrators. While the CALSPEC sources use independently derived spectral templates, the HST calibration is also fundamentally referenced to a Vega model which is similar to the fundamental calibration used for IRAC; therefore, it is possible that both calibrations have a similar systematic bias. Our earlier analysis showed the S17 IRAC calibration agreed with the HST CALSPEC based calibration to within the uncertainties (2%). A revised analysis using the final cryogenic calibration results in a much smaller bias in the CALSPEC comparison with all IRAC bands in agreement between the two photometric systems to better than 1% when the white dwarfs are ignored for the 5.8 and 8.0 μm bands. The white dwarf photometry for the Si:As arrays is extremely noisy due to the faintness of the white dwarfs at longer wavelengths. In addition, the long wavelength data were taken using in-place repeats which introduced a systematic bias in the repeat photometry due to residual per-pixel pattern noise on the array due to imperfect array bias subtraction.

The flux conversions from the solar analogs are midway between the AV and KIII values suggesting that all three types of sources are appropriate to within current uncertainties for mid-infrared calibration as are the white dwarf stars although they are faint for current generation instruments. The small CALSPEC bias suggests that decision to average over the AV and KIII calibrators was reasonable and that final IRAC calibration minimizes systematic errors that do not depend on the fundamental flux scaling from Vega/Sirius.

5. SUMMARY AND FUTURE DIRECTIONS

The final cryogenic IRAC calibration leverages all of the calibration data collected throughout the duration of the mission as well as knowledge of the shape of the intra-pixel gain variation from warm mission data. The final calibration uses a simultaneous solution of the photometric variation across the field of view and the intra-pixel gain to provide photon-noise limited photometry of more than 10000 points for each IRAC band reducing the measurement errors to negligible values. Using revised spectral templates, the KIII stars were folded back into the solution with the resulting calibration having a total error of <2.5% in all bands and agreeing to better than 1% with an independent calibration using the HST CALSPEC templates. The use of KIII, AV, white dwarfs and solar analogs in mid-infrared calibration has been verified and we recommend using a synthesis of these different types of calibrators to minimize the systematics inherent in any one given calibrator type.

Table 3. Final cryogenic calibration. For each band, we list the final cryogenic flux conversion in units of MJy/sr / (DN/s), σ_m, the statistical uncertainty in the flux conversion, σ_{zero}, the uncertainty in the fundamental calibration stars, the bias between the flux conversion determined by the A dwarfs only and the K giants only, and the bias between the calibration and a calibration determined using the HST calspec data basis. For the 5.8 and 8.0 μm bands, two values are given for the CALSPEC bias. The first value is the bias using all of the CALSPEC observed sources. The value in parenthesis is the bias without the white dwarf photometry.

Band	FLUXCONV	σ_m	σ_{zero}	A-K bias	CALSPEC bias
3.6	0.1069	0.6%	1.5%	-1.79%	0.4%
4.5	0.1382	0.5%	1.5%	-1.25%	-0.3%
5.8	0.5858	0.6%	1.5%	0.48%	-3.9% (-0.3%)
8.0	0.2026	0.6%	1.5%	-1.39%	-1.2% (-0.7%)

The calibration of mid-infrared telescopes is currently fundamentally limited by the 1.5% uncertainty in the fundamental calibration of celestial sources to terrestrial standards through the transfer of NIST standards to observations of Vega and Sirius. New spectrophotometric observations of fundamental and primary infrared calibrators using a NIST calibrated telescope[22] are currently planned. These observations are being done in conjunction with warm IRAC observations of the same standards as well as HST WFC3 spectrometry[23] of those calibrators. In particular, observations of Sirius and 109 Vir can be directly compared to a recently developed synthetic zero magnitude flux standard[24]. Observations of the fundamental calibrators with Spitzer and Hubble are extremely challenging as these sources are extremely bright and outside of the nominal dynamic range of the instrumentation on these telescopes. For the IRAC observations, a technique where the source is observed so that the core of the PRF is saturated and a high-fidelity model of the extended PSF is fit to the wings of the profile is used. This technique[25] has been shown to provide photometry accurate to 1%. Sufficient sources exist that the technique can be used on sources which can also be observed in the IRAC subarray mode, providing a direct mapping of the saturated source fitting of fundamental calibrators to the standard IRAC photometry.

It is very probable that with improved observations of fundamental calibrators as well as improved modeling and analysis of potential systematics in the various types of calibrators that an absolute calibration of better than 1% in the infrared can be realized enabling a wide range of science with current and future observatories such as JWST.

ACKNOWLEDGEMENTS

REFERENCES

[1] Fazio, G. G., Hora, J. L., Allen, L. E., Ashby, M. L. N., Barmby, P., Deutsch, L. K., Huang, J.-S., et al., "The Infrared Array Camera (IRAC) for the *Spitzer* Space Telescope," ApJS, 154, 10-17 (2004).

[2] Hora, J. L., Fazio, G. G., Allen, L. E., Ashby, M. L. N., Barmby, P., Deutsch, L. K., Huang, J.-S., et al., "In-flight performance and calibration of the Infrared Array Camera (IRAC) for the *Spitzer* Space Telescope," Proc. SPIE 5487, 77-92 (2004).

[3] Werner, M. N., Roellig, T. L., Low, F. J., Rieke, G. H., Rieke, M., Hoffmann, W. F., Young, E., et al., "The *Spitzer* Space Telescope Mission," ApJS, 154, 1-9 (2004).

[4] Carey, S. J., Surace, J. A., Glaccum, W. J., Ingalls, J., Krick, J., Lacy, M., Lowrance, P., et al., "Calibration and data quality of warm IRAC," Proc. SPIE 7731, 77310N-77310N-15 (2010).

[5] Tinetti, G., Vidal-Madjar, A., Liang, M.-C., Beaulieu, J.-P., Yung, Y., Carey, S., Barber, R. J., et al., "Water vapour in the atmosphere of a transiting extrasolar planet," Nature, 448, 169-171 (2007).

[6] Knutson, H. A., Charbonneau, D., Allen, L. E., Fortney, J. J., Agol, E., Cowan, N. B., Showman, A. P., et al., "A map of the day-night contrast of the extrasolar planet HD 189733b," Nature, 447, 183-186, (2007).

[7] Stanford, S. A., Brodwin, M., Gonzalez, A. H., Zeimann, G., Stern, D., Dey, A., Eisenhardt, P. R., et al., "IDCS J1426+3508: Discovery of a Massive, IR-Selected Galaxy Cluster at z = 1.75," ApJ, 753, 164 (2012).

[8] Yan, H., Finkelstein, S. L., Huang, K.-H., Ryan, R. E., Ferguson, H. C., Koekemoer, A. M., Grogin, N. A., et al., "Luminous and High Stellar Mass Candidate Galaxies at z~8 Discovered in CANDELS," ApJL submitted, arXiv:1112.6406 (2011).

[9] Zheng, W., Postman, M., Zitrin, A., Moustakas, J., Shu, X., Jouvel, S., Host, O., et al., "A highly magnified candidate for a young galaxy seen when the Universe was 500 Myrs old," arXiv, arXiv:1204.2305 (2012).

[10] Carey, S., Surace, J., Lacy, M., Glaccum, W., Lowrance, P., Hora, J. L., and Willner, S. "Stability of the Infrared Array Camera for the *Spitzer* Space Telescope," Proc. SPIE 7010, 70102V-70102V-8 (2008).

[11] Weinberg, D. H., Mortonson, M. J., Eisenstein, D. J., Hirata, C., Riess, A. G., Rozo, E., "Observational Probes of Cosmic Acceleration," arXiv:1201.2434 (2012).

[12] Freedman, W. L., Madore, B. F., Scowcroft, V., Monson, A., Persson, S. E., Seibert, M., Rigby, J. R., et al., "The Carnegie Hubble Program," AJ, 142, 192-201 (2011).

[13] Meng, H. Y. A., Rieke, G. H., Su, K. Y. L., Ivanov, V. D., Vanzi, L., Rujopakarn, W., "Variability of the Infrared Excess of Extreme Debris Disks," ApJL, 751, 17 (2012).

[14] Brinkworth, C. S., Gänsicke, B. T., Girven, J. M., Hoard, D. W., Marsh, T. R., Parsons, S. G., Koester, D., "A Spitzer Space Telescope Study of the Debris Disks around Four SDSS White Dwarfs," ApJ, 750, 86-92 (2012).

[15] Reach, W. T., Megeath, S. T., Cohen, M., Hora, J., Carey, S., Surace, J., Willner, S. P., et al., "Absolute Calibration of the Infrared Array Camera on the Spitzer Space Telescope," PASP, 117, 978-990 (2005).

[16] Cohen, M., Megeath, S. T., Hammersley, P. L., Martín-Luis, F., Stauffer, J., "Spectral Irradiance Calibration in the Infrared. XIII. ``Supertemplates" and On-Orbit Calibrators for the SIRTF Infrared Array Camera," AJ, 125, 2645-2663 (2003).

[17] Engelke, C. W., Price, S. D., Kraemer, K. E., "Spectral Irradiance Calibration in the Infrared. XVI. Improved Accuracy in the Infrared Spectra of the Secondary and Tertiary Standard Calibration Stars," AJ, 132, 1445-1463 (2006).

[18] Ingalls, J., Krick, J. E., Carey, S. J., Laine, S., Surace, J. A., Glaccum, W. J., et al., "Intra-pixel gain variations and high-precision photometry with the InfraRed Array Camera (IRAC)," Proc SPIE 8442, 8442-68 (2012).

[19] Hora, J. L., Carey, S., Surace, J., Marengo, M., Lowrance, P., Glaccum, W. J., Lacy, M., et al., "Photometry using the Infrared Array Camera on the Spitzer Space Telescope," PASP, 120, 1233-1243 (2008).

[20] Quijada, M. A., Marx, C. T., Arendt, R. G., Moseley, S. H., "Angle-of-incidence effects in the spectral performance of the infrared array camera of the *Spitzer* Space Telescope," Proc. SPIE 5487, 244-252, (2004).

[21] Bohlin, R. C., Gordon, K. D., Rieke, G. H., Ardila, D., Carey, S., Deustua, S., Engelbracht, C., et al., "Absolute Flux Calibration of the IRAC Instrument on the Spitzer Space Telescope Using Hubble Space Telescope Flux Standards," AJ, 141, 173-(2011).

[22] Kaiser, M. E., Morris, M., Hart, M., McCandliss, S. R., Rauscher, B., J., Kimble, R. A., Kruk, J. W., et al., "ACCESS: design and test performance," Proc. SPIE 8442, 8442-156 (2012).

[23] Deustua, S., "Vega and the absolute calibration of HST," Proc. SPIE 8442, 8442-114 (2012).

[24] Engelke, C. W., Price, S. D., Kraemer, K. E., "Spectral Irradiance Calibration in the Infrared. XVII. Zero-magnitude Broadband Flux Reference for Visible-to-infrared Photometry," AJ, 140, 1919-1928 (2010).

[25] Marengo, M., Stapelfeldt, K., Werner, M. W., Hora, J. L., Fazio, G. G., Schuster, M. T., Carson, J. C., et al., "Spitzer/Infrared Array Camera Limits to Planetary Companions of Fomalhaut and epsilon Eridani," ApJ, 700, 1647-1657 (2009).